AFRL-AFOSR-VA-TR-2019-0074

Carrier Based Long Wavelength Electromagnetic Light Bullets, Carrier Shock Initiated Exotic Waveforms and Extreme NLO Pulse Delivery to Targets
Extreme NLO Pulse Delivery to Targets

Jerome Moloney
UNIVERSITY OF ARIZONA

03/13/2019
Final Report

Air Force Research Laboratory
AF Office Of Scientific Research (AFOSR)/ RTB1
Arlington, Virginia 22203
Air Force Materiel Command

DISTRIBUTION A: Distribution approved for public release.

REPORT DOCUMENTATION PAGE

Form Approved
OMB No. 0704-0188

1. REPORT DATE *(DD-MM-YYYY)*	2. REPORT TYPE	3. DATES COVERED *(From - To)*
15-03-2019	Final Performance	15 Dec 2015 to 14 Dec 2018

4. TITLE AND SUBTITLE
Carrier Based Long Wavelength Electromagnetic Light Bullets, Carrier Shock Initiated Exotic Waveforms and Extreme NLO Pulse Delivery to Targets Extreme NLO Pulse Delivery to Targets

5a. CONTRACT NUMBER

5b. GRANT NUMBER
FA9550-16-1-0088

5c. PROGRAM ELEMENT NUMBER
61102F

6. AUTHOR(S)
Jerome Moloney

5d. PROJECT NUMBER

5e. TASK NUMBER

5f. WORK UNIT NUMBER

7. PERFORMING ORGANIZATION NAME(S) AND ADDRESS(ES)
UNIVERSITY OF ARIZONA
888 N EUCLID AVE RM 510
TUCSON, AZ 85719-4824 US

8. PERFORMING ORGANIZATION REPORT NUMBER

9. SPONSORING/MONITORING AGENCY NAME(S) AND ADDRESS(ES)
AF Office of Scientific Research
875 N. Randolph St. Room 3112
Arlington, VA 22203

10. SPONSOR/MONITOR'S ACRONYM(S)
AFRL/AFOSR RTB1

11. SPONSOR/MONITOR'S REPORT NUMBER(S)
AFRL-AFOSR-VA-TR-2019-0074

12. DISTRIBUTION/AVAILABILITY STATEMENT
A DISTRIBUTION UNLIMITED: PB Public Release

13. SUPPLEMENTARY NOTES

14. ABSTRACT
The main thrust of this effort was to build a new fundamental theory of LWIR intense ultrashort pulse (USPL) propagation in condensed and gaseous media. A new canonical description of pulse propagation captured by a generalized modified Kadomtsev-Petviashili (MkP) equation. The UPPE equation was extended to include the full HITRAN linear atmospheric refractive index (dispersion) and absorption database. We implemented a 1D/2D bi-directional version of UPPE to address to important problems: 1) reflection of internally generated backward fields or 2) counter-propagating E.M pulses in finite length nonlinear samples. We discovered that microscopic many-body effects introduce a new paradigm for the long range delivery of high energy self-trapped LWIR 10 micron pulses. Moreover, the classical avalanche ionization model does not correctly capture ionization at these long wavelengths and we introduced a new two-temperature model that supported recent joint UCLA-Brookhaven National Laboratory experiment. We concluded a preliminary investigation of the role of nonlinear contributions of clusters of detuned rovibrational transitions in modifying the HITRAN linear response allowing us to explore its impact albeit over few hundred meter propagation ranges. We also implemented a new stable fully anisotropic and semi-conformal FDTD solver and applied it to novel plasmonic and high index dielectric metamaterials.

15. SUBJECT TERMS
LIR light bullets, NLO light matter interaction

16. SECURITY CLASSIFICATION OF:			17. LIMITATION OF ABSTRACT	18. NUMBER OF	19a. NAME OF RESPONSIBLE PERSON
a. REPORT	b. ABSTRACT	c. THIS PAGE			NACHMAN, ARJE

Standard Form 298 (Rev. 8/98)
Prescribed by ANSI Std. Z39.18

Unclassified	Unclassified	Unclassified	UU	**PAGES**	**19b. TELEPHONE NUMBER** *(Include area code)* 703-696-8427

FINAL REPORT

To: technicalreports@afosr.af.mil and http://afosr.reports.sgizmo.com/s3/>
Subject: Final Progress Statement to Dr. Arje Nachman

Contract/Grant Title: Carrier Based Long Wavelength Electromagnetic Light Bullets, Carrier Shock Initiated Exotic Waveforms and Extreme NLO Pulse Delivery to Targets

Contract/Grant #: FA9550-16-1-0088

Reporting Period: December 15, 2015 – December 14, 2018

Accomplishments (200 words max):

The main thrust of this effort was to build a new fundamental theory of LWIR intense ultrashort pulse (USPL) propagation in condensed and gaseous media. A new canonical description of pulse propagation captured by a generalized modified Kadomtsev-Petviashili (MkP) equation. The UPPE equation was extended to include the full HITRAN linear atmospheric refractive index (dispersion) and absorption database. We implemented a 1D/2D bi-directional version of UPPE to address to important problems: 1) reflection of internally generated backward fields or 2) counter-propagating E.M pulses in finite length nonlinear samples. We discovered that microscopic many-body effects introduce a new paradigm for the long range delivery of high energy self-trapped LWIR 10 μm pulses. Moreover, the classical avalanche ionization model does not correctly capture ionization at these long wavelengths and we introduced a new two-temperature model that supported recent joint UCLA-Brookhaven National Laboratory experiment. We concluded a preliminary investigation of the role of nonlinear contributions of clusters of detuned rovibrational transitions in modifying the HITRAN linear response allowing us to explore its impact albeit over few hundred meter propagation ranges. We also implemented a new stable fully anisotropic ε and μ semi-conformal FDTD solver and applied it to novel plasmonic and high index dielectric metamaterials.

Archival publications (published) during reporting period:

Kevin Werner, Michael G. Hastings, Aaron Schweinsberg, Brian L. Wilmer, Drake Austin, Cristopher M. Wolfe, Miroslav Kolesik, Trenton R. Ensley, Laura Vanderhoef, Anthony Valenzuela, and Enam ChowdhuryUltrafast mid-infrared high harmonic and supercontinuum generation with n_2 characterization in zinc selenide" Optics Express Vol 27, No. 3, 2867-2885 (2019)

V.E. Babicheva and J. Moloney, "Lattice Zenneck modes on subwavelength antennas," Laser & Photonics Reviews 12, 1800267 (2019).

P.D. Terekhov, V.E. Babicheva, K. Baryshnikova, A. Shalin, A. Karabchevsky, A. B. Evlyukhin, "Multipole analysis of dielectric metasurfaces and lattice invisibility effect," Physical Review B 99, 045424 (2019).

"Megafilament in air formed by self-guided terawatt long-wavelength infrared laser" Sergei Tochitsky, Eric Welch1, Mikhail Polyanskiy, Igor Pogorelsky, Paris Panagiotopoulos, Miroslav Kolesik, Ewan M. Wright, Stephan W. Koch, Jerome V. Moloney, Jeremy Pigeon and Chan Joshi, Nature Photonics, 13, 41, 2019

David Juhasz, Miro Kolesik, and Per Kristen Jakobsen "Convergence and completeness for square-well Stark resonant state expansions"JOURNAL OF MATHEMATICAL PHYSICS 59, 113501 (2018).

J. Lee, Y. Arita, S. Toyoshima, K. Miyamoto, P. Panagiotopoulos, E. M. Wright, K. Dholakia, and T. Omatsu, "Photopolymerization with Light Fields Possessing Orbital Angular Momentum: Generation of Helical Microfibers," ACS Photonics 5, 4156-4163 (2018)

Nehls J, Dineen C, Liu J, Poole C, Brio M, Moloney JV. Stable 3D FDTD method for arbitrary fully-electric and magnetic anisotropic Maxwell's equations. *Int J Numer Model*. 2018;e2521. https://doi.org/10.1002/jnm.2521

V.E. Babicheva and J. Moloney, "Lattice effect influence on the electric and magnetic dipole resonance overlap in a disk array," Nanophotonics 7(10), 1663-1668 (2018).

V.E. Babicheva and A.B. Evlyukhin, "Resonant suppression of light transmission in high-refractive-index nanoparticle metasurfaces," Optics Letters 43(21), 5186-5189 (2018).

V.E. Babicheva, "Lattice effect in Mie-resonant dielectric nanoparticle array under the oblique light incidence," MRS Communications, doi.10.1557/mrc.2018.216 (2018).

V.E. Babicheva, "Lattice Kerker effect in the array of hexagonal boron nitride antennas," MRS Advances 3, 2783-2788 (2018).

V.E. Babicheva and A.B. Evlyukhin, "Interplay and coupling of electric and magnetic multipole resonances in plasmonic nanoparticle lattices," MRS Communications 8, 712-717 (2018).

P. Rosenow, M. Kolesik, S. W. Koch, J. V. Moloney, "Effective nonlinear rovibrational response of water vapor for efficient pulse propagation simulations", J. Opt. Soc. Am. B, in press (2018).

F. H. M. Faisal and S. Förster "Coulomb-Volkov S-matrix theory of ionization" Journal of Physics B, 51, 234001 (2018)

Hofstrand A. , Moloney J. V. "Modeling ultrashort electromagnetic pulses with a generalized Kadomtsev-Petviashvili equation" Physica D – Nonlinear Phenomena, 366, 51 (2018)

Schuh, Kolja; Panagiotopoulos, Paris; Kolesik, Miroslav; Koch, Stephan; Moloney, Jerome "Multi-terawatt 10 mu m pulse atmospheric delivery over multiple Rayleigh ranges", Optics Letters, 42, 3722 (2017)

K. Schuh, M. Kolesik, E. M. Wright, J. V. Moloney, S. W. Koch "Self-Channeling of High-Power Long-Wave Infrared Pulses in Atomic Gases" Physical Review Letters 118, 063901 (2017)

K. Schuh, P. Rosenow, M. Kolesik, E. M. Wright, S. W. Koch, J. V. Moloney, "Nonlinear rovibrational polarization response of water vapor to ultrashort long-wave infrared pulses" Physical Review A 96, 043818 (2017)

U. Huttner, K. Schuh, J. V. Moloney, and S. W. Koch, "Similarities and differences between high-harmonic generation in atoms and solids", J. Opt. Soc. Am. B **33**, C22-C29 (2016)

Paris Panagiotopoulos, Kolja Schuh, Miroslav Kolesik and Jerome V. Moloney, “Simulations of 10 μm filaments in a realistically modeled atmosphere”, Journal of the Optical Society of America B, 33, 2154 (2016)

Paris Panagiotopoulos, Miroslav Kolesik and Jerome Moloney “Exploring the limits to energy scaling and distant-target delivery of high-intensity midinfrared pulses”, Physical Review A, **94**, 033852 (2016)

F. H. M Faisal “Strong-field *S*-matrix theory with final-state Coulomb interaction in all orders”, Physical Review A, 94, 031401 (2016)

Accepted/Submitted:

Aihua Lin, Per Kristen Jakobsen, “A 3D Nonlinear Maxwell's Equations Solver Based On A Hybrid Numerical Method”, Submitted to Physica Scripta, October 2018.

“Memory effects in the long-wave infrared avalanche ionization of gases: A review of recent progress" by Wright, Ewan; Koch, Stephan; Kolesik, Miroslav; Moloney, Jerome Reports on Progress in Physics

Talks Given:

2016

PQE, Jerome V. Moloney “High-Power Mid-IR Atmospheric Light Bullets”, Snowbird, Utah

University College Cork, Jerome V. Moloney, “Long Range Robust Multi-Terawatt Mid-IR Atmospheric Light Bullets" at Tyndall Institute, Ireland

COFIL 2016, Jerome V. Moloney “Long Range Robust Multi-Terawatt Mid-IR Atmospheric Light Bullets" Quebec, Canada

University College Cork, Jerome V. Moloney “Long Range Robust Multi-Terawatt Mid-IR Atmospheric Light Bullets” Cork, Ireland

Applied Physics Dept, Dept of Mathematics, University of Arizona, Jerome V. Moloney “Long Range Mid-IR Atmospheric Light Bullets”, Arizona

COFIL 2016, Miroslav Kolesik, “Metastable electronic state approach to light-matter interactions in optical filametation”, Montreal, Canada

SPIE Defense + Commercial Sensing Conference, Miroslav Kolesik, Modeling ultrafast lase pulse propagation, Baltimore

2017

PQE 2017: Physics of Quantum Electronics: "Long Range Atmospheric Transport of Multi-TW Ultrashort mid-IR Pulses", P. Panagiotopoulos, K. Schuh, J. V. Moloney, M. Kolesik and S.W Koch.

University of Central Florida, Jerome V. Moloney "New Paradigm for multi-TW MWIR and LWIR Atmospheric Propagation over Kilometer Ranges", Orlando, Florida

University of Marburg, Jerome V. Moloney "Nonlinear confinement of multi-teraWatt Ultrashort laser pulses over Kilometer ranges", Germany

Heriot-Watt University, Jerome V. Moloney "Nonlinear propagation of multi-tera Watt mid and long wave ultrashort laser pulses over kilometer ranges" Edinburgh, Scotland

University of Vermont, Jerome V. Moloney "Nonlinear transport of multi-terawatt mid and long wave ultrashort electromagnetic light bullets over kilometer ranges", Vermont

OSA Nonlinear Optics Conference, Miroslav Kolesik, "Metastable electronic state approach for nonlinear response in atoms and molecules: Experiment-theory comparison", Hawaii

2018

2018 MRS Fall Meeting & Exhibition V. Babicheva and J.V. Moloney, "Lattice Resonances with Localized Zenneck Modes," Boston, MA

Conference on Lasers and Electro-Optics (CLEO), V. Babicheva, A.B. Evlyukhin, J.M. Nehls, C. Dineen, and J.V. Moloney, "Control of Electric and Magnetic Resonances in Nanoparticle Metasurfaces,", San Jose, CA

2018 MRS Spring Meeting & Exhibition, V. Babicheva and A. Evlyukhin, "Kerker effect with Collective Multipole Resonances in Nanoparticle Lattices", Phoenix, AZ

DEPS 2018: Directed Energy Professional Society: "E-field resolved simulations of long wavelength mid-IR TW ultrashort pulses over kilometer ranges in realistically modeled atmosphere", Paris Panagiotopoulos, P. Rosenow, M. Kolesik, and J.V. Moloney.

UBP III: Ultrafast Bandgap Photonics III: "Simulation of LWIR TW ultrashort pulses over kilometer ranges in the atmosphere", P. Panagiotopoulos, P. Rosenow, K. Schuh, M. Kolesik, E. M. Wright, S. W. Koch, and J. V. Moloney.

AFOSR Forum, Jerome V. Moloney "Singularity driven Kilometer range TeraWatt Atmospheric Light Bullets", Washington, DC

AFOSR 2018 Annual Review of Theoretical NLO Contactors, Jerome V. Moloney "Ultrashort LWIR TeraWatt Pulse Atmospheric Propagation and Interactions with Interfaces", Washington, DC

Jerome V. Moloney "Physics of Ultrashort LWIR TeraWatt Pulse Atmospheric Propagation and Interactions" Glasgow, Scotland

COFIL 2018, Jerome V. Moloney “Mid-IR Filamentation”, Switzerland

COFIL 2018, Andrew M. Hofstrand, “The interaction of intense, ultrashort laser pulses with remote targets”, Switzerland

SIAM Conference, Andrew M. Hofstrand, “Modeling ultrashort electromagnetic pulses with a generalized Kadomtsev-Petviashvili equation” Anaheim, CA

ONR MURI Meeting, Jerome V. Moloney “LWIR Nonlinear Optics in gases: Theory and Simulation”, University of Maryland, MD

COFIL 2018, Miroslav Kolesik, “Resonant-state description of light-matter interaction in optical filaments”, Geneva, Switzerland

Changes in research objectives, if any: None

Changes in AFOSR program manager, if any: None

Extensions granted or milestones slipped, if any: None

Include any new discoveries, inventions or patent disclosures during this reporting period (if none, report none): none

Final Technical Report: FA9550-15-1-0088

Contract/Grant Title: Carrier Based Long Wavelength Electromagnetic Light Bullets, Carrier Shock Initiated Exotic Waveforms and Extreme NLO Pulse Delivery to Targets

Reporting Period: December 15, 2015 – December 14, 2018

Technical Summary

The main thrust of this 3 year effort was to build on preliminary discoveries made near the endpoint of a previous MURI and transition these discoveries into a new fundamental theory of mid-IR and LWIR intense ultrashort pulse (USPL) propagation in condensed and gaseous media. One of the key observations of the current project was the inadequacy of nonlinear envelope modes of all flavors in capturing the physics of extreme nonlinear optics (NLO) and instead, the need for full optical carrier resolved unidirectional pulse propagators. Instead of a NLSE-type description, a new canonical description of pulse propagation is captured by a generalized modified Kadomtsev-Petviashili (MkP) equation. The relevant generalization involved in extending this model to ultrabroadband general dispersions characteristic of realistic media. Our computational workhorse remains the UPPE equation, first proposed by us in 2002, and now extended to include the full HITRAN linear atmospheric refractive index (dispersion) and absorption database directly in the solver. Despite these added complexities we were able to simulate high intensity (energy) LWIR pulses over multiple kilometer distances. The final open problem that we addressed was how to implement a bi-directional version of UPPE to address to important problems: 1) reflection of internal nonlinear generation of backward fields or 2) counter-propagating E.M pulses on interrogating finite length nonlinear samples.

Another important research breakthrough of this project was the discovery that microscopic many-body effects, extensively studied in condensed media (semiconductors), can introduce a new paradigm for the delivery of high energy whole beam self-trapped propagation of LWIR 10 μm light bullets over tens of Rayleigh ranges. Furthermore, we discovered that the classical avalanche ionization model, extensively employed to understand plasma generation from USPs, does not correctly capture of ionization at these long wavelengths. We introduced a new two temperature model that was further corroborated by a recent experiment involving a joint UCLA-Brookhaven National Laboratory and published in Nature Photonics in January 2019. A final breakthrough in the LWIR propagation study, was the preliminary investigation of the role of nonlinear contributions of the huge clusters of detuned rovibrational transitions to modify the HITRAN linear response. A computationally feasible effective nonlinear HITRAN model allowed us to explore its impact albeit over shorter few hundred meter propagation ranges.

Parallel supported investigations included the implementation of a new semi-conformal FDTD solver that we showed to be stable for fully anisotropic in ε and μ materials. This new algorithm was developed to handle grid meshing conformal locally to regions of multiple arbitrarily shaped objects while preserving the global Cartesian meshing. The latter allows for efficient parallel scaling using our

earlier developed Cartesian grid codes. This project also investigated novel plasmonic and high index dielectric metamaterial applications with a focus on planar structures.

Mathematical Models: UPPE and BPPE

The full vectorial optical carrier resolved bidirectional pulse propagation equation (BPPE) below, was formulated by us early on but no attempt was made to implement it until very recently.

$$\partial_z \vec{E}^{\perp}_{k_x,k_y,+}(\omega,z) = +ik_z \vec{E}^{\perp}_{k_x,k_y,+}(\omega,z) + \sum_{s=1,2} \vec{e}_s^{\perp}\vec{e}_s^{\perp}.[\frac{i\omega^2}{2\epsilon_0 c^2 k_z}\vec{P}_{k_x,k_y}(\omega,z) - \frac{\omega}{2\epsilon_0 c^2 k_z}\vec{J}_{k_x,k_y}(\omega,z)]$$

$$\partial_z \vec{E}^{\perp}_{k_x,k_y,-}(\omega,z) = -ik_z \vec{E}^{\perp}_{k_x,k_y,+}(\omega,z) - \sum_{s=1,2} \vec{e}_s^{\perp}\vec{e}_s^{\perp}.[\frac{i\omega^2}{2\epsilon_0 c^2 k_z}\vec{P}_{k_x,k_y}(\omega,z) - \frac{\omega}{2\epsilon_0 c^2 k_z}\vec{J}_{k_x,k_y}(\omega,z)]$$

$$k_z(\omega,k) \equiv \sqrt{\omega^2 \varepsilon(\omega)/c^2 - k^2}$$

The ± subscripts refer to forward and backward propagating vector fields with the latter being Fourier resolved in time (ω) and transverse spatial coordinates (k_x, k_y). The propagation direction is along the z-axis. The first terms on the RHS of both equations encapsulate the full linear response of the medium in question and as we will see below, captures the HITRAN spectral response of air over many decades of frequency. The polarization and current source terms will include all nonlinear effects such as Kerr, Raman, microscopic many-body etc. With these turned off, both equations can be trivially integrated in z. The BPPE equations are essentially a Maxwell-level propagator but with nonparaxial counterpropagating fields primarily confined to large angles in the forward/backward direction. As we shall see, they are marked improvements on Maxwell solvers such as FDTD as the latter are confined to very small computational domains in 3D.

The scalar unidirectional approximation to BPPE has become the simulation standard or investigating extreme NLO events in condensed and gaseous media.

$$\partial_z \mathscr{E}(z,\omega,k) = ik_z(\omega,k)\mathscr{E}(z,\omega,k) + \frac{i\omega^2}{2\varepsilon_0 c^2 k_z(\omega,k)}\mathscr{P}(z,\omega,k) - \frac{\omega}{2\varepsilon_0 c^2 k_z(\omega,k)}\mathscr{J}(z,\omega,k)$$

An explicit example of a classical real space polarization source is given below.

$$P(z,r,t) = \varepsilon_0 \Delta\chi_{\mathrm{sf}}(z,r,t)E(z,r,t) = 2\varepsilon_0 \bar{n}_2 \left[\frac{1}{2}E^2(z,r,t) + \frac{1}{2}\int_0^{\infty} R(\tau)E^2(z,r,t-\tau)\mathrm{d}\tau\right]E(z,r,t)$$

This includes an instantaneous Kerr and delayed Raman response with the latter accounting for molecular rotations. The main outcome of the present research project has been to identify additional nonlinear sources and currents that can seed long wavelength intense pulses propagating in diverse condensed and gaseous media.

The great strength of UPPE (and BPPE) is the ability to capture realistic linear (and nonlinear) responses over huge spectral bandwidths. This is crucial in any extreme NLO setting as spectral responses remote

from the fundamental driving field prove crucial in phase-matching nonlinear generation of harmonics, for example, or in the other limit near DC THz fields. Moreover, the broad featureless generated supercontinuum makes it impossible to partition the problem into separate spectral windows and implement coupled nonlinear envelope models describing individual harmonic generation.

Figure 1 below shows the HITRAN linear response for air from short wavelengths to beyond 12 µm. The complicated transmittance and susceptibility incorporates all relevant air constituents (O_2, N_2, CO_2 ,H_2O etc) where individual curves refer to different humidity levels.

Illustrated with down arrows for a 10µm fundamental wavelength are the third and fifth harmonic and remote THz spectral locations that need to be accurately captured in simulations.

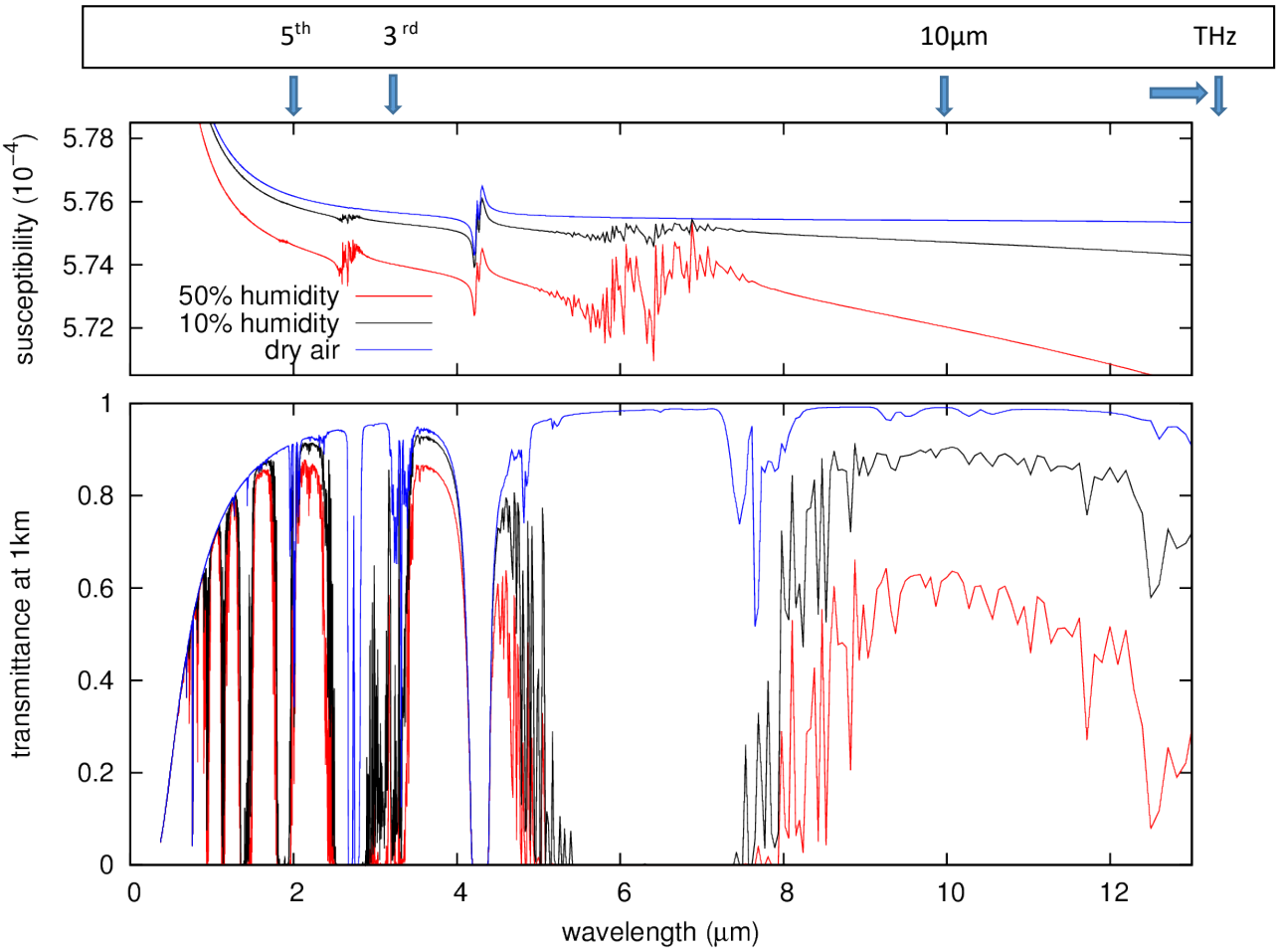

Figure 1 HITRAN database for the atmosphere.

The sensitivity of the nonlinear response to the presence and concentration of different atmospheric species in air is dramatically illustrated below by a blow-up of the HITRAN response around 4µm in the mid-IR. Removing CO_2 from the database dramatically changes the asymptotic behavior of a propagating pulse. Adding CO_2 introduces a strong absorption feature near 4.6µm and the dispersion is changes from being normal to anomalous over a broad spectral range below that resonance. The end result is that a USP propagating near, say 3.7µm, will now undergo compression in time.

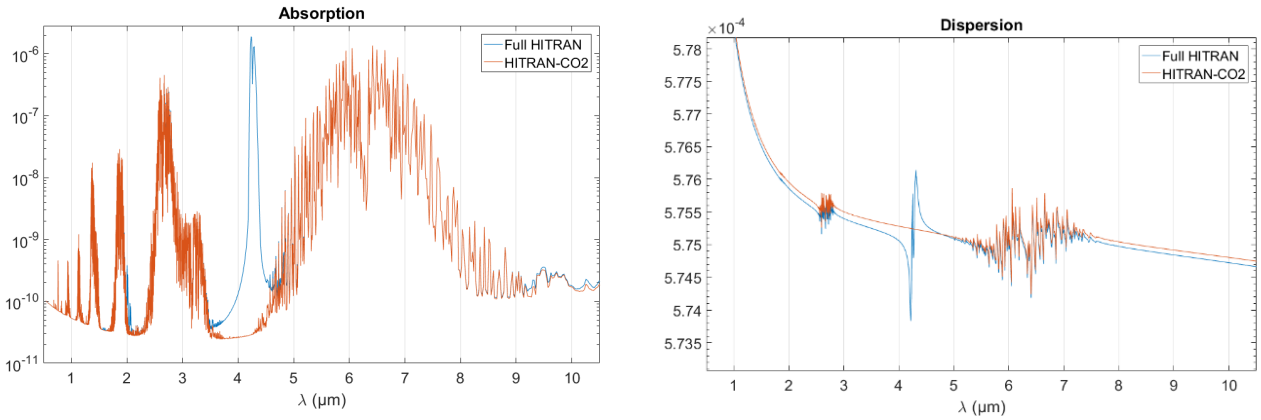

Figure 2. Blow-up of HITRAN database in the mid-IR window around 4 μm. Removing the CO_2 species fundamentally changes the linear response as shown in red.

Modified Kadomtsev-Petviashili (mKP): Canonical Description of Long Wave Propagation

The UPPE description of USP propagation is universal and applies to near-IR and long wavelengths. However, it is rather opaque when it comes to mathematically investigating key properties such as collapse etc. In the long wavelength limit we pointed out earlier that the NLSE-type and all envelope models fail and it becomes necessary to include the full optical carrier wave, primarily due to the need to include the underlying optical carrier wave self-steepening that becomes important in regularizing the self-focusing collapse singularity at mid-IR and longer wavelengths. We showed earlier that the modified Kadomtsev Petvisahili (mKP) equation is the appropriate mathematical description. This model was extended by Ph.D student, Andrew Hofstrand, to include more general nonlinearity and dispersion with the latter more appropriate to capture realistic air properties over a wider spectral landscape [Hofstrand 2018]. The generalized KP (gKP) model is derived directly from the UPPE model and placed in a rigorous mathematical setting. A first version of this work appears in: Hofstrand A. , Moloney J. V. "Modeling ultrashort electromagnetic pulses with a generalized Kadomtsev-Petviashvili equation" Physica D – Nonlinear Phenomena, 366, 51 (2018). A follow-up paper analyzing the gKp has been submitted to Physica Scripta.

The gKP equation:

$$\partial_t\left[\partial_z E+\sum_{j=1}^{N}(-1)^j\epsilon_{\text{disp},j}\partial_t^{2j+1}E+n(n-1)\epsilon_{\text{nl}}E^{n-2}\partial_t E\right]=\epsilon_{\text{diff}}\Delta_\perp E$$

has the following conserved quantities:

$$\mathcal{H}[E]=-\frac{1}{2}\sum_{j=1}^{N}\epsilon_{\text{disp},j}\int_{\mathbb{R}^{d+1}}\left(\partial_t^j E\right)^2 dtdx+\frac{1}{2}\epsilon_{\text{diff}}\int_{\mathbb{R}^{d+1}}\left|\partial_t^{-1}\nabla_\perp E\right|^2 dtdx-\epsilon_{\text{nl}}\int_{\mathbb{R}^{d+1}}E^n dtdx$$

The Hamiltonian or energy

$$\mathcal{P}[E]=\int_{\mathbb{R}^{d+1}} E^2 dtdx$$

the power

$$\mathcal{V}[E]=\frac{1}{2}\int_{\mathbb{R}^{d+1}} x^2 E^2 dtdx$$

and, a higher order moment.

Assuming that E becomes singular at finite Z and defining

$$X_j \equiv \frac{x_j}{(Z-z)^{\beta}}, \quad T \equiv \frac{\tau-\tau^*}{(Z-z)^{\gamma}}, \quad E(z,\mathbf{x},\tau)=\frac{1}{(Z-z)^{\alpha}}F(\mathbf{X},T)$$

One can show, using the conserved quantities, that one can obtain a formula for the critical exponent for a general anomalous dispersion. In fact, we note, here that in the case of an intense pulse propagating through a Kerr medium with only anomalous, $(2\zeta+1)$-order dispersion, the result can be generalized giving the expected critical exponent

$$n-2=\frac{4\zeta}{(\zeta+1)d+1}$$

This relates the order of the nonlinearity in gKP to the order of the anomalous dispersion. Figure 3 below encapsulates this general behavior for different dimensions d.

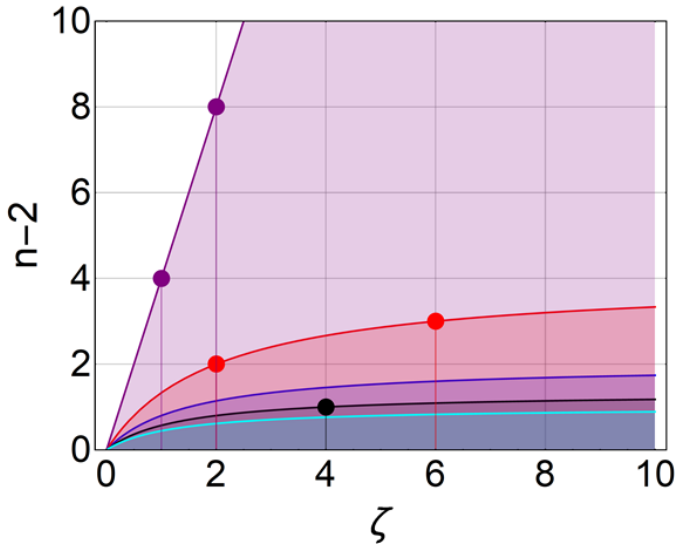

Figure 3 Critical collapse: $(2\zeta+1)$-order anomalous dispersion versus $(n-1)$-order nonlinearity with transverse dimension $d=0$ (purple), $d=1$ (red), $d=2$ (blue), $d=3$ (black), and $d=4$ (cyan). The shaded areas are subcritical regions in each dimension and the marked points on the critical curves are integer solutions of the above relation.

Figure 4 below shows a series of simulations of propagating pulse waveforms in various dimensions d.

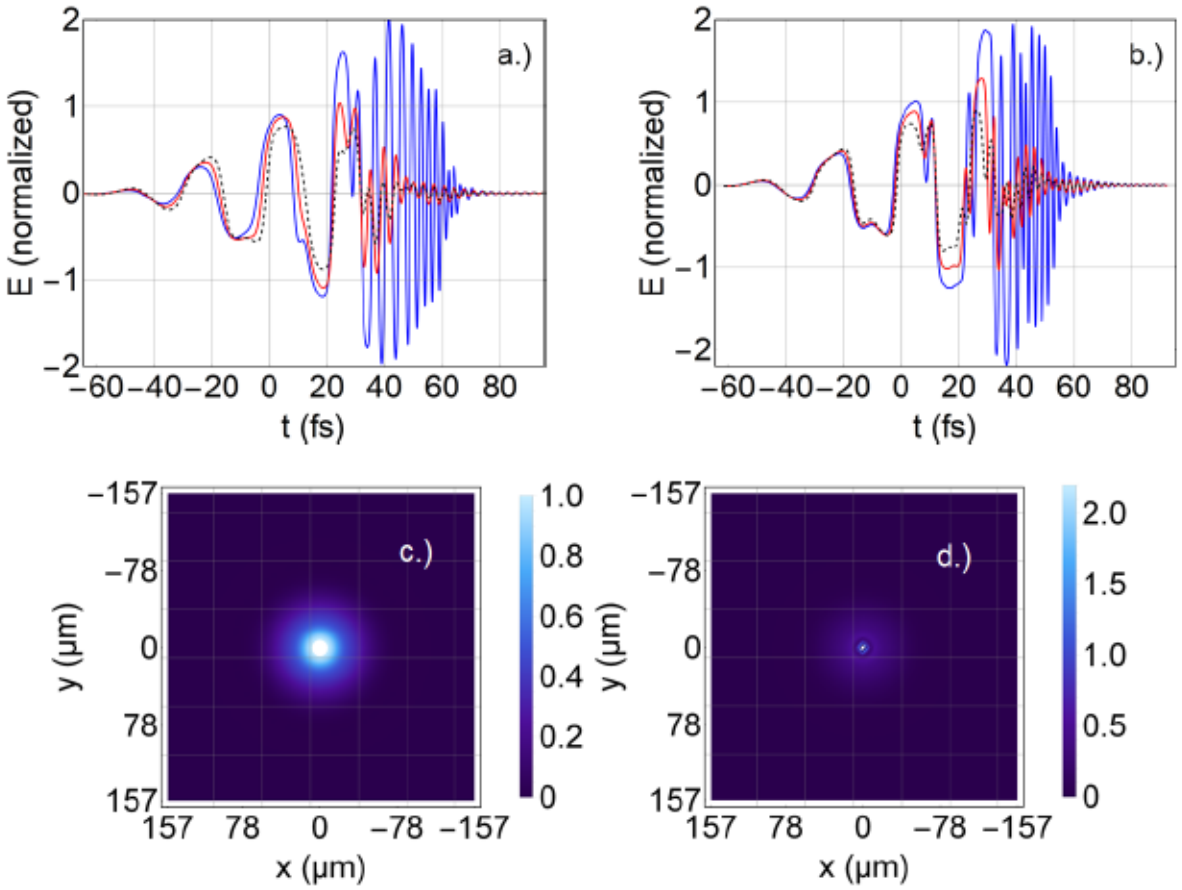

Figure 4 Critical collapse: $(2\zeta+1)$ *-order anomalous dispersion versus* $(n-1)$ *-order nonlinearity with transverse dimension* $d=0$ *(purple),* $d=1$ *(red),* $d=2$ *(blue),* $d=3$ *(black), and* $d=4$*. The shaded areas are subcritical regions in each dimension and the marked points on the critical curves are integer solutions of relation of the above relation.*

Bidirectional Pulse Propagation Equation (BPPE)

The bidirectional propagation equations are simplified here to just include nonlinear polarization sources. The formulation also extends to include current sources. The full optical carrier resolved forward $A_+(z,\omega,\mathbf{k}_\perp)$ and backward $A_-(z,\omega,\mathbf{k}_\perp)$ fields are directly coupled through the nonlinear polarization.

$$\partial_z A_+(z,\omega,\mathbf{k}_\perp) - i\beta(\omega,\mathbf{k}_\perp)A_+(z,\omega,\mathbf{k}_\perp) = \frac{i\omega^2}{2c^2\beta(\omega,\mathbf{k}_\perp)} P_{\mathrm{NL}}[E](z,\omega,\mathbf{k}_\perp)$$

$$\partial_z A_-(z,\omega,\mathbf{k}_\perp) + i\beta(\omega,\mathbf{k}_\perp)A_-(z,\omega,\mathbf{k}_\perp) = -\frac{i\omega^2}{2c^2\beta(\omega,\mathbf{k}_\perp)} P_{\mathrm{NL}}[E](z,\omega,\mathbf{k}_\perp)$$

$$\beta(\omega,\mathbf{k}_\perp) = \sqrt{n^2(\omega)\omega^2/c^2 - |\mathbf{k}_\perp|^2}$$

The dispersion relation $\beta(\omega,\mathbf{k}_\perp)$ again encapsulates to full linear absorption/dispersion as for example, in the HITRAN database. For the example treated here the nonlinear polarization $P_{\mathrm{NL}}[E](z,\omega,\mathbf{k}_\perp)$ will be a Kerr nonlinearity cubic in the full field.

An additional degree of freedom in solving this system is the integral constraint.

$$A_-(z_0,\omega,\mathbf{k}_\perp) = \int_{z_0}^{Z^*} \partial_z A_+(z,\omega,\mathbf{k}_\perp) e^{2i\beta z} dz = \frac{i\omega^2}{2c^2\beta} \int_{z_0}^{Z^*} P_{\mathrm{NL}}[A_+](z,\omega,\mathbf{k}_\perp) e^{i\beta z} dz$$

An iterative scheme, assuming a relatively weak backscatterd filed, to solve this system using a "shooting" method is summarized below:

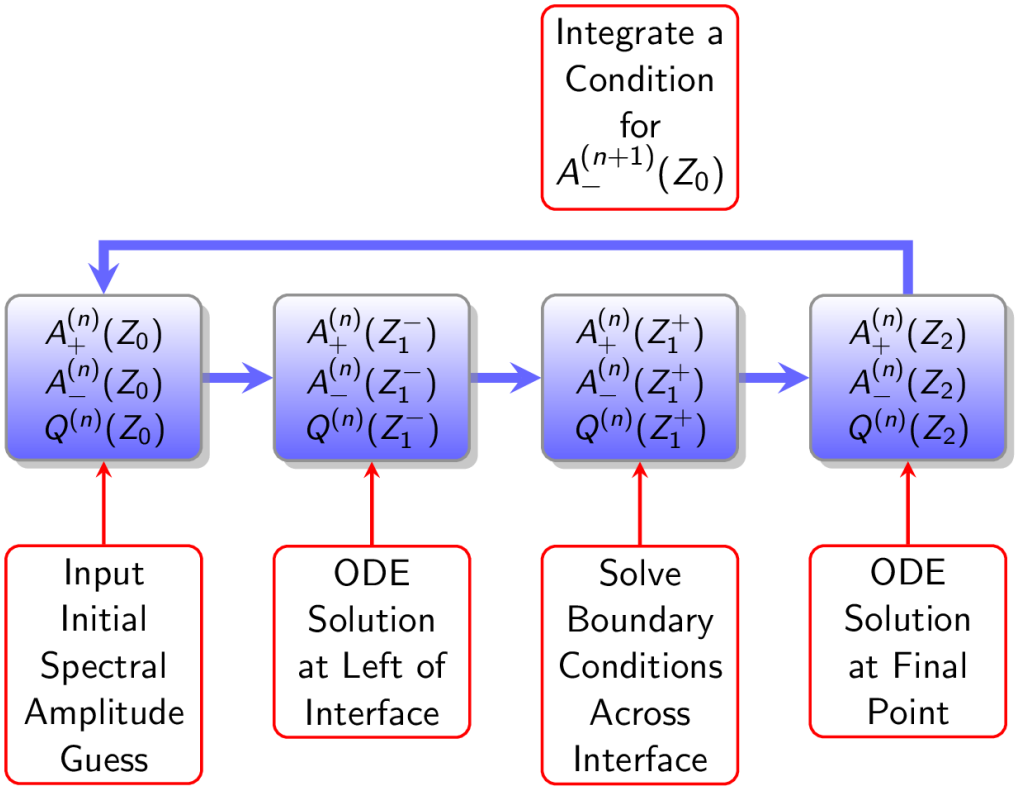

A preliminary result of the application of BPPE is a 1D simulation of two co-propagating pulses, one at the fundamental and the second at the second harmonic is shown in Fig. 5 below. The interaction of

these pulses generates a THz pulse remote from the optical driving fields. This result and other 2D test results have been verified to FDTD solutions to the full Maxwell equations in small computational domains. We clearly observe accumulation of numerical dispersive errors in the FDTD solution even at very high resolution.

The ongoing plan is to continue the development of a general BPPE solver that can be efficiently parallelized in 3D + time. This will be a major task although alleviated by the acquisition of a new state of the art HPE Superdome Flex supercomputer with AFOSR DURIP support. We are also extending the method to implement two strong counter-propagating pulses with arbitrary central carrier frequencies.

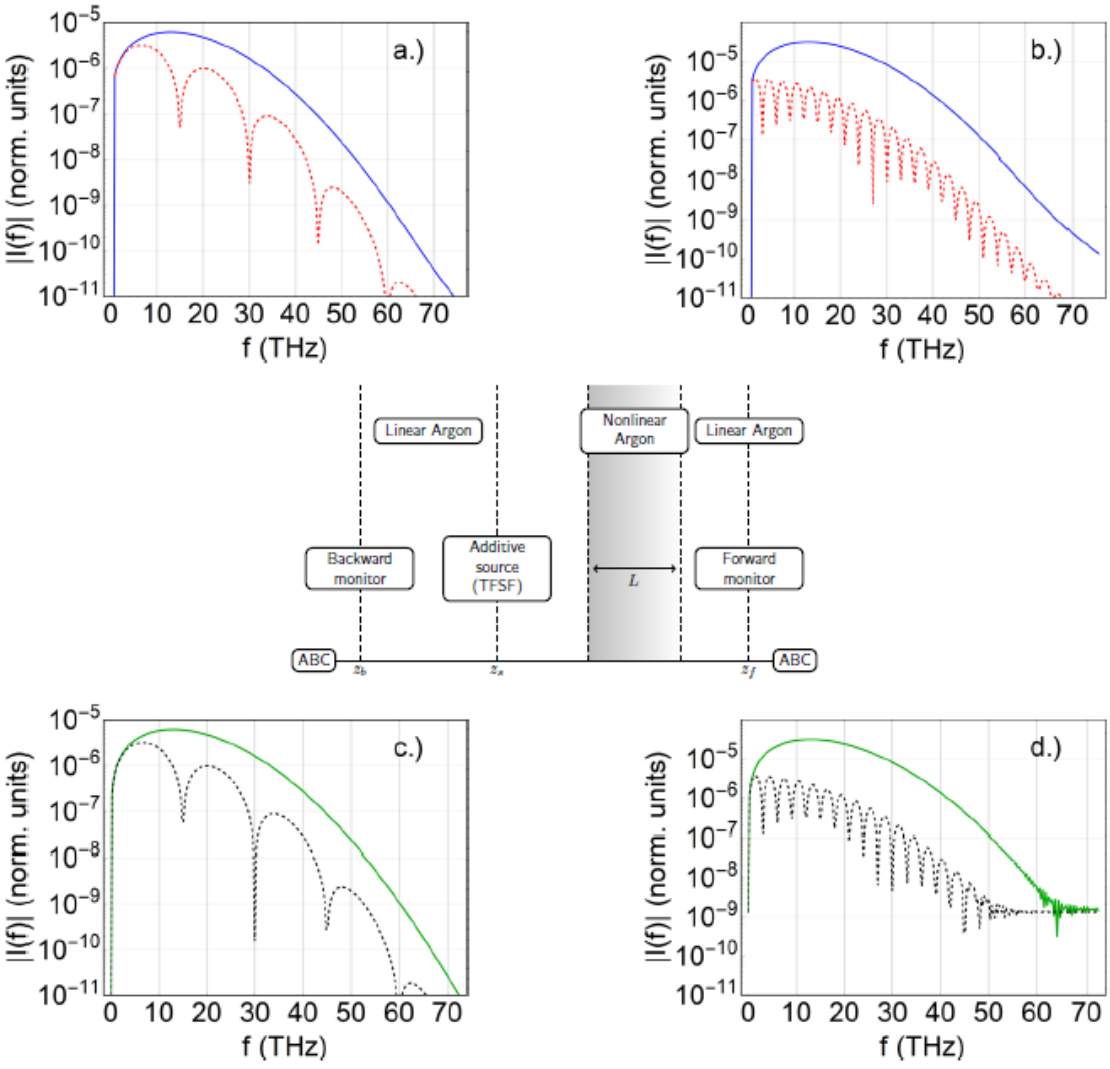

Figure 5. Generated THz spectra for forward and backward generated fields. Top: Iterative BPPE solution. Center: Setup of the computational domain and Bottom: corresponding full Maxwell results. The high frequency oscillations on the backward THz spectrum depend on nonlinear domain thickness.

Highly Detuned Semiconductor and Air Many-body Response

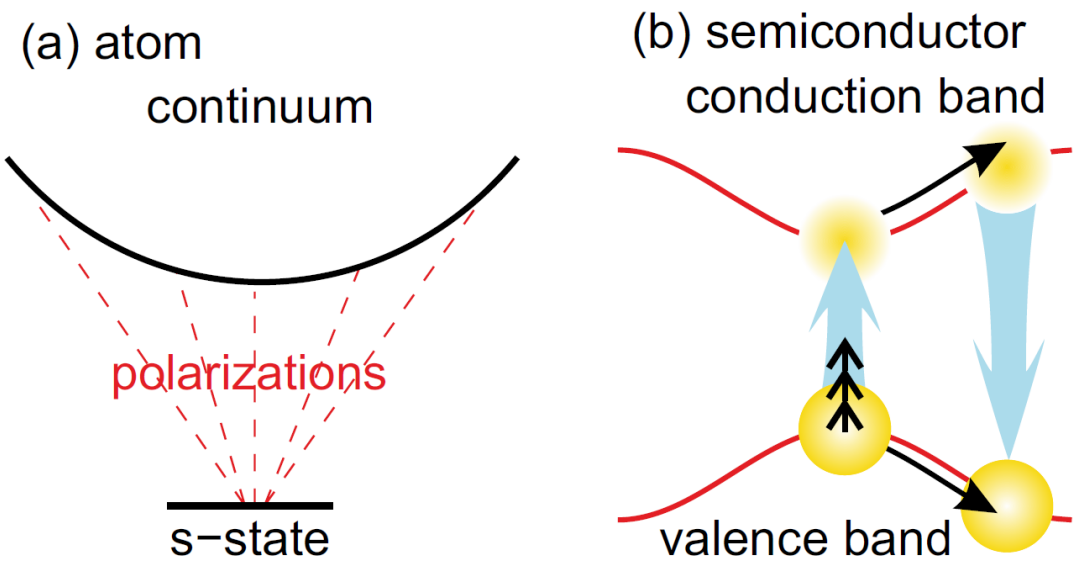

The physics of light matter coupling changes fundamentally, relative to resonant or near resonant interactions, when the incident light field is strongly detuned from resonance at longer wavelengths. In this limit, there is a close mathematical connection between a detuned semiconductor and a dilute gas as we shall see below. The schematic above shows a simple atomic level description (a) and a corresponding semiconductor (b) where it is assumed that the long wavelength optical field is strongly detuned from the indicated transitions in both cases. Essentially, the semiconductor conduction band is now the (multi-atom) continuum.

The zeroth order Hamiltonians describing either the two band semiconductor or the multi-atom bound state –continuum is given by:

$$H_0 = \sum_{\vec{k}} \left(\varepsilon^e_{\vec{k}} a^\dagger_{c,\vec{k}} a_{c,\vec{k}} + \varepsilon^h_{\vec{k}} a^\dagger_{v,\vec{k}} a_{v,\vec{k}} \right) \quad \text{- semiconductor}$$

$$H_0 = \sum_i \varepsilon_s a^\dagger_{s,i} a_{s,i} + \sum_{\vec{k}} \varepsilon^e_{\vec{k}} a^\dagger_{\vec{k}} a_{\vec{k}} \quad \text{- gas}$$

The zeroth order Hamiltonian captures the single particle properties of the relevant media (valence and conduction band for the semiconductor and bound states and continuum for the gas). The quantum operators $a^{\dagger}_{s,i}$, $a_{s,i}$ represent particle creation and annihilation operators. Here k refers to the free particle momentum (in the bands or continuum) and the index i in the second term represents the sum over atom bound states. The interaction Hamiltonian that couples the system to the driving is given by

$$H_D = i\,|\,e\,|\,E(t)\sum_{\lambda,\vec{k}} a^{\dagger}_{\lambda,\vec{k}}(\nabla_{\vec{k}} a_{\lambda,\vec{k}}) - \sum_{k} E(t)(a^{\dagger}_{c,k} a_{v,k} d_{cv} E(t) + c.c.) \qquad \text{- semiconductor}$$

$$H_D = i\,|\,e\,|\,E(t)\sum_{\vec{k}} a^{\dagger}_{\vec{k}}(\nabla_{\vec{k}} a_{\vec{k}}) - \sum_{i,k} \Omega_{s,\vec{k}} a^{\dagger}_{s,i} a_{\vec{k}} + \Omega_{s,\vec{k}} a^{\dagger}_{\vec{k}} a_{s,i}) \qquad \text{- gas}$$

where

$$\Omega_{s,\vec{k}} = \vec{d}_{s,\vec{k}} E(t)$$

is the Rabi frequency.

The first term, marked in red, is the intraband coupling term and describes the acceleration of free carriers by the field across momentum states within respective bands or continuum. The contribution of this term is negligible in resonant media and is usually ignored. The contribution common to both is the interband term that describes electric dipole optical transitions between individual bands or states.

The next order contributions to the Hamiltonian are the correlation terms:

$$H_{el-el} = \frac{1}{2}\sum_{q,k,k'} a^{\dagger}_{\vec{k}} a^{\dagger}_{\vec{k}'} a_{\vec{k}+\vec{q}} a_{\vec{k}'-\vec{q}} W(q)$$

This four operator term describes higher order correlations between carriers (electrons, holes) within respective bands (continuum) and is an intrinsic material property – the driving E field does not explicitly appear in it. It is responsible in semiconductor lasers for kinetic hole filling and, as w e will see here for so-called Excitation Induced Dephasing (EID) in a detuned semiconductor or a gas. $W(q)$ is the screened Coulomb potential – strongly screened for a semiconductor but essentially unscreened for a gas.

We showed in paper by U. Huttner, K. Schuh, J. V. Moloney, and S. W. Koch, "Similarities and differences between high-harmonic generation in atoms and solids", J. Opt. Soc. Am. B **33**, C22-C29 (2016), the close analogy and differences between higher harmonic generation in a detuned semiconductor and a gas. The main observed difference is a symmetry breaking in a semiconductor due to the presence of an additional valence band (light and heavy hole) that facilitates the generation of all (even and odd) harmonics of the driving field. Moreover, the intraband terms in the interaction Hamiltonian are responsible for driving carriers (electrons and holes) across the Brillouin zone in contrast to the atomic system where transitions are limited to narrow k-bands.

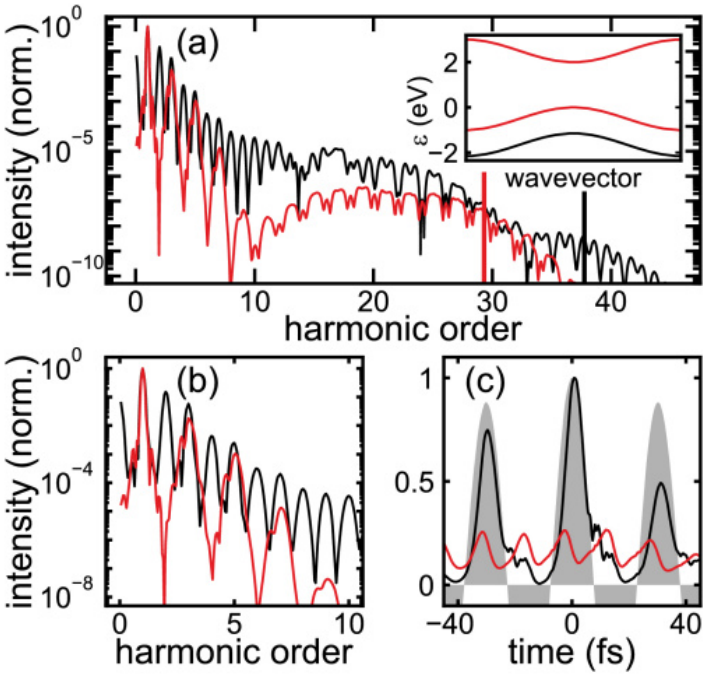

Figure 6 contrasts HHG in a two-band vs a three-band semiconductor. The red curves for the two-band model exhibit odd harmonics in direct analogy with the gas. Introduction of a third band gives rise to the black HHG spectrum where even and odd harmonics are prominent.

A preliminary publication on harmonic generation and measurement of the Kerr coefficient in polycrystalline solids involving a collaboration with ARL scientists and Ohio State experimental collaborators has just appeared in Optics Express. Kevin Werner, Michael G. Hastings et al., "Ultrafast mid-infrared high harmonic and supercontinuum generation with n_2 characterization in zinc selenide" Optics Express Vol 27, No. 3, 2867-2885 (2019) involved Michael Hastings, a Ph.D student in the group carrying out the simulations. The physics of these materials is poorly understood because of the random arrangements on micro sized crystals in the material.

The microscopic many-body equations of motion derived from the above Hamiltonians for both a detuned semiconductor and atomic gas are quite similar so we only reproduce the gas version here. They describe the interaction between a ground state (and possibly higher bound states) and continuum as depicted in Fig. 2(a) above

$$i\hbar\frac{d}{dt}f_s = \sum_{\vec{k}}\Omega^*_{s\vec{k}}P^*_{s\vec{k}} - \Omega_{s\vec{k}}P_{s\vec{k}}$$

$$i\hbar\frac{d}{dt}f_{\vec{k}} = N\left[\Omega_{s\vec{k}}P_{s\vec{k}} - \Omega^*_{s\vec{k}}P^*_{s\vec{k}}\right] - \frac{e}{\hbar}\vec{\nabla}_{\vec{k}}f_{\vec{k}}\vec{E}$$

$$i\hbar\frac{d}{dt}P_{s\vec{k}} = \left[\varepsilon_s - \varepsilon_{\vec{k}}\right]P_{s\vec{k}} + \Omega^*_{s\vec{k}}\left[f_{\vec{k}} - f_s\right] - \frac{e}{\hbar}\vec{\nabla}_{\vec{k}}P_{s\vec{k}}\vec{E} + \sum_{\vec{k}'\neq\vec{k}}\Omega^*_{s\vec{k}'}P_{\vec{k}'\vec{k}} + i\hbar\frac{d}{dt}P_{s\vec{k}}\Big|_{\text{e-e}}$$

$$i\hbar\frac{d}{dt}P_{\vec{k}\vec{k}'} = \left[\varepsilon_{\vec{k}} - \varepsilon_{\vec{k}'}\right]P_{\vec{k}\vec{k}'} - \frac{e}{\hbar}\vec{\nabla}_{\vec{k}}P_{\vec{k}\vec{k}'}\vec{E} + \Omega_{s\vec{k}}P_{s\vec{k}'} - \Omega^*_{s\vec{k}'}P^*_{s\vec{k}}$$

If we ignore the term $i\hbar\frac{d}{dt}P_{s\vec{k}}|_{\text{e-e}}$ in the third equation, these dynamical terms for bound and continuum populations and polarizations describe the coherent driving of an individual atom (molecule) by the external driving field. In the case of highly detuned driving, one would observe a transient excitation of "virtual" electrons into continuum states with a complete return of the excitation to the ground state after the pulse has passed. This process is termed ultrafast Adiabatic Following (AF) and has been verified previously in atomic gases and semiconductors.

The missing term $i\hbar\frac{d}{dt}P_{s\vec{k}}|_{\text{e-e}}$ is derived from the correlation Hamiltonian and is responsible for interrupting the phase coherence of the dynamically induced nonlinear polarization in the third equation. This "escape from adiabatic following" is referred to as Excitation Induced Dephasing (EID) and is responsible for leaving small concentrations of residual excited electrons in the continuum (weak plasma). This microscopic many-body theory was developed systematically by us in a series of earlier papers and supported under an earlier AFOSR MURI.

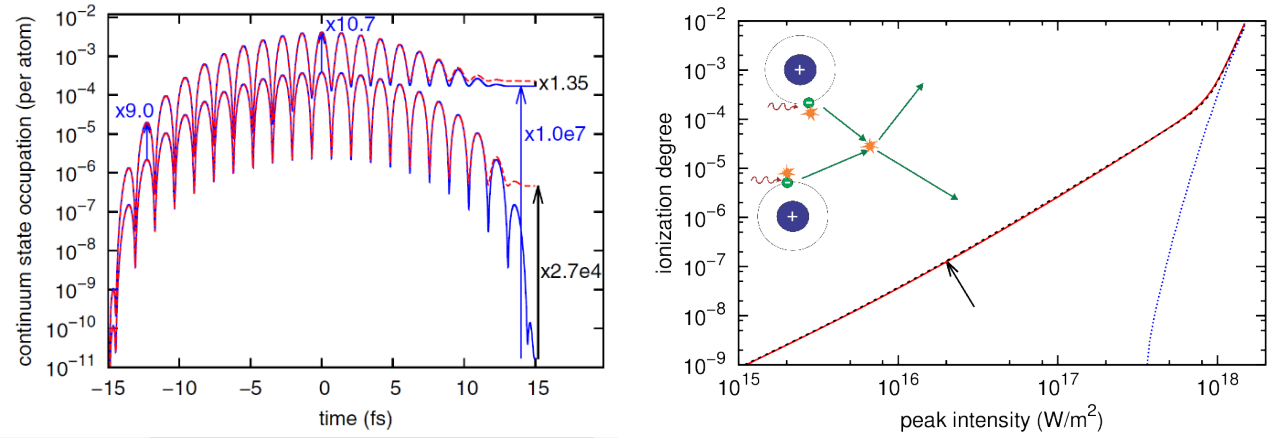

Figure 7 *shows the transient excitation of electrons into continuum states with and without the correlation term switched on. At lower intensities, corresponding to the arrow location on the right, the "virtual" excited electrons undergo AF in the absence of correlation terms and are returned to the ground state after being driven by a 30 fs pulse (blue lower curve). If the interaction terms are switched on, a small residual population of electrons is left behind in the continuum (red lower curve). This corresponds to the ionization degree shown by the arrow on the right plot. This weak ionization occurs well below the single electron ionization threshold depicted by the blue dotted curve in the right figure. The microscopic lower intensity ionization fundamentally changes the paradigm for long wavelength (10μm) atmospheric propagation as we shall see later.*

For completeness, our microscopic many-body simulations include not just changes in populations due to electron-electron scattering but also due to electron-ion and electron-neutral scattering as given below.

$$\frac{\partial}{\partial t} f_{\vec{k}}\Big|_{\text{Coul}}^{\text{el-el}} = -\frac{2\pi}{\hbar} \sum_{\vec{k}',\vec{q}} \delta(\epsilon_{\vec{k}} + \epsilon_{\vec{k}'} - \epsilon_{\vec{k}+\vec{q}} - \epsilon_{\vec{k}'-\vec{q}}) \left[f_{\vec{k}} f_{\vec{k}'} - f_{\vec{k}+\vec{q}} f_{\vec{k}'-\vec{q}} \right] |V_q|^2$$

$$\frac{\partial}{\partial t} f_{\vec{k}}\Big|_{\text{Coul}}^{\text{el-ion}} = -N_{\text{ion}} \frac{2\pi}{\hbar} \sum_{\vec{q}} \delta(\epsilon_{\vec{k}} - \epsilon_{\vec{k}+\vec{q}}) |V_q|^2 \left[f_{\vec{k}} - f_{\vec{k}+\vec{q}} \right]$$

$$\frac{\partial}{\partial t} f_{\vec{k}}(t)|^{\text{el-n}} = -N_n \frac{2\pi}{\hbar} \sum_{\vec{q}} \delta(\epsilon_{\vec{k}} - \epsilon_{\vec{k}+\vec{q}}) W_n^2(k,q) \left[f_{\vec{k}}(t) - f_{\vec{k}+\vec{q}}(t) \right]$$

These microscopic theory results are included as additional sources coupling to the external field in the long range atmospheric propagation simulations that we discuss next. It does become necessary to approximate the full model by a simpler effective model that accurately captures the behavior exhibited in Fig. 5 (right-hand side figure).

Microscopic Many-Body Kerr Lens Suppression – Nonlinear Self-trapped Pulses

The microscopic many-body theory summarized above is a key underpinning for a new paradigm that supports whole beam self-trapping rather than filamentation for pulses of few picosecond duration. This theory enabled the simulation of high power and energy USPs over few kilometer ranges in air. Very favorable to multi-TW and multi-Joule pulse sustenance over multiple kilometers the known scaling of the critical power with wavelength

$$P_{\text{crit}} = \frac{0.3\lambda^2}{nn_2}$$

This scaling with λ^2 means that a 10μm pulse has the potential to carry more than two orders of magnitude greater power than an 800nm near-IR filament. Given that P_{crit} for an 800nm pulse is estimated to lie between 5 and 10 GW, a 10μm pulse should support on the order of a TW or more in an individual filament. However, the onset of filamentation (collapse singularity) is severe, leading to optical carrier shock regularization at mid-IR and longer wavelengths and consequently to relatively early termination of the filament at tens of meters propagation distance.

Some form of nonlinear confinement of the beam cross-section is necessary to offset the detrimental effects of strong diffraction at such long wavelengths. An important consequence of weak microscopically generated plasma is that it can systematically suppress the usual instantaneous (or delayed) Kerr nonlinearity and reduce the self-focusing lensing effect. Moreover, it is straightforward to deduce from the microscopic theory the following scaling of plasma polarization and electron population with wavelength:

$$P_{\text{pl}} = -f(t)\frac{e^2\mu_0}{m}\lambda^2 E \qquad\qquad n_{\text{pl}} = -f(t)\frac{e^2\mu_0}{2m}\lambda^2$$

Where f(t) is the driving pulse envelope.

Figure 6 illustrates this Kerr lends suppression and contrasts its impact for 300 fs and 3 ps 10µm pulses. The usual "instantaneous" Kerr contribution tracking the pulse envelope is shown in mauve in both pictures. The 30 fs pulse data is shown on the left and 3 ps on the right. The microscopic plasma contribution is shown by the green curve in both cases and the black curve shows the net dynamical Kerr contribution (difference of mauve and green curves).

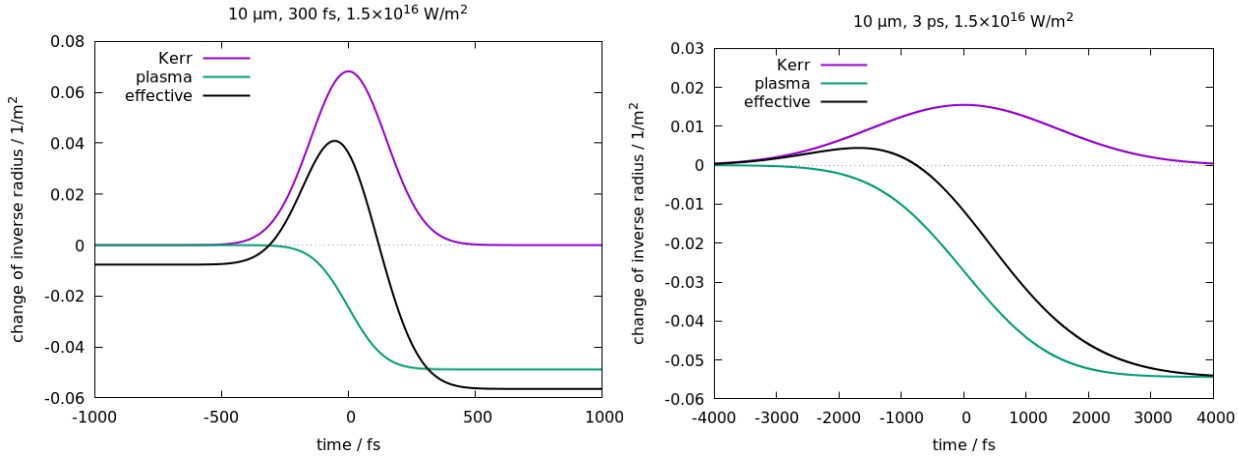

Figure 8. Left: Kerr lens suppression by microscopically generated plasma for a 10 µm 30 fs pulse at a peak intensity of 1.5x10^{16} W m^{-2}. Right: Kerr lens suppression by microscopically generated plasma for a 10 µm 3 ps pulse with a peak intensity of 1.5x10^{16} W m^{-2}.

It is evident on comparing these two figures that the Kerr lens suppression is a strong function of pulse duration with a much weaker dynamical lens for the longer 3 ps pulse. It also shows that longer pulses generate more free electrons towards the leading edge of the pulse.

We now summarize some important results that support the idea that a self-trapped pulse rather than a filament is better for delivering high power and high energy pulses at range. In the publication [K. Schuh, M. Kolesik, E. M. Wright, J. V. Moloney, S. W. Koch "Self-Channeling of High-Power Long-Wave Infrared Pulses in Atomic Gases" Physical Review Letters 118, 063901 (2017)], we showed for the first time that self-trapped multi TW and Joule pulses can propagate over multiple kilometer range. Our simulations were necessarily confined to radial symmetry because of computational complexity and are shown in Figure 9.

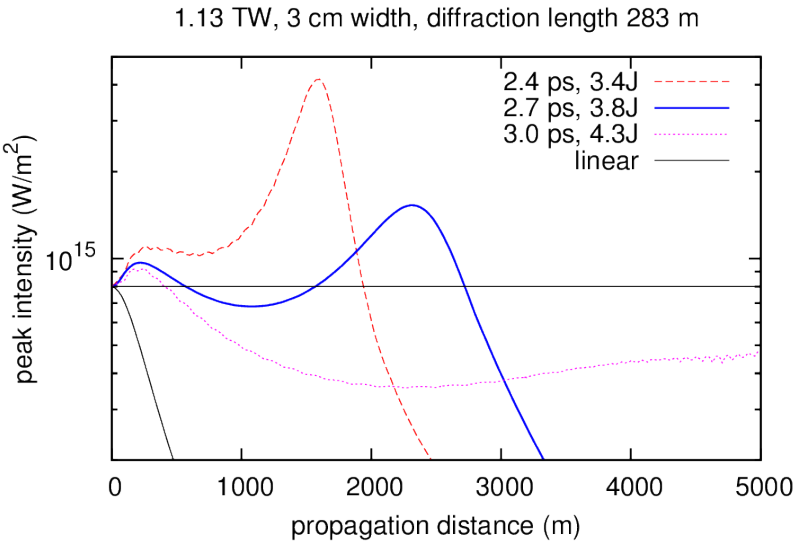

Figure 9 plots the peak intensity versus propagation distance for different pulse durations and at the same peak power. Increasing the pulse duration from 2.4 ps to 3.0 ps scales up the energy from 3.4 J to 4.3 J and greatly elongates the propagation scale. While the 3 ps pulse initially undergoes a drop in peak intensity (pink dotted curve) it recovers and says self-trapped over the full 5 km range indicated. A linear pulse will have diffracted over about 300 meters (black curve). This picture supports our belief that many-body induced weaker but positive Kerr lenses support self-trapping over filamentation and allows for transport of multi TW powers and multiple Joule energies

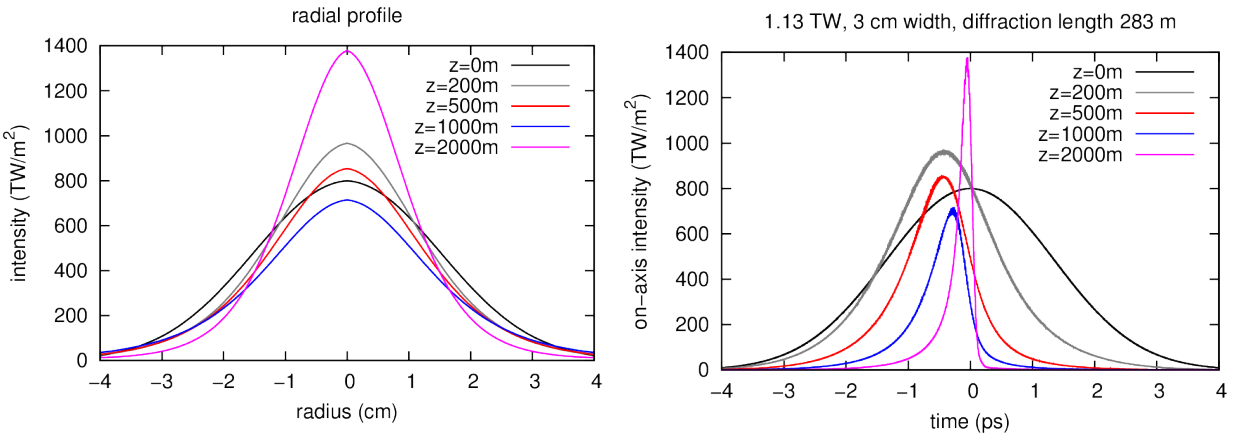

Figure 10 further supports whole beam self-trapping where the transverse profile of the beam is shown at different propagation distances corresponding to the blue curve shown in Fig. # above. A filament would involve strong spatial compression with the filament lying on top of a broad beam (energy reservoir). Instead, we observe a slight drop in peak intensity followed by a gradual spatial compression of the beam. The maximum compression of the whole beam is observed around d 2.5 km.

Figure 10 (Left) shows a gradual spatial compression of the beam signifying that the mechanism is self-trapping rather than abrupt filamentation. Temporal compression of the pulse (Figure 10 (right)) is much

more dramatic. The initial 3 ps pulse compresses down to about 150 fs as a consequence of a very broad anomalous spectral window centered at 10 µm.

The simulations above used a simple Argon model for the propagation medium as the goal was to isolate the new physics without the complexity of multiple species as in air. The next phase was to introduce a realistic atmosphere with the linear spectral response described by the full HITRAN database (shown in Fig. 1).

Fig. 11 shows radial symmetry simulations in air for different pulse durations ranging from 2.4 ps to 3 ps. Included in addition, is a simulation with the microscopic physics turned off (no MB). The latter shows two much stronger and earlier intensity bursts more common with filamentation and the field dies off relatively quickly. In this case, optical carrier shock regularization limits the unbounded intensity growth. Again, the longer pulse is sustained over a 5 km distance.

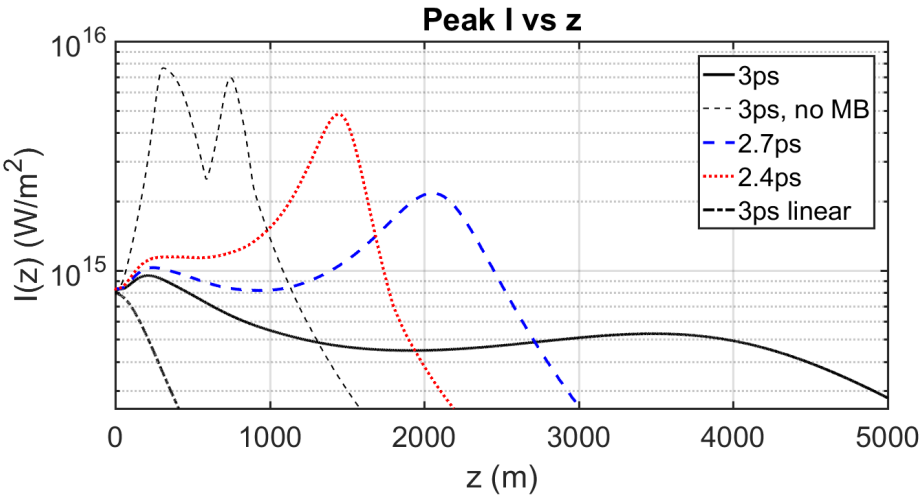

Figure 11 shows the evolution of the peak intensity of pulses of different durations 2.4 ps, 2.7 ps and 3 ps in a realistic HITRAN atmosphere. The corresponding linear result (dash-dots) shows a Rayleigh range of around 300m. The dashed black curve corresponds to a case where the microscopic many-body ionization is switched off and shows evident of a double filamentray burst.

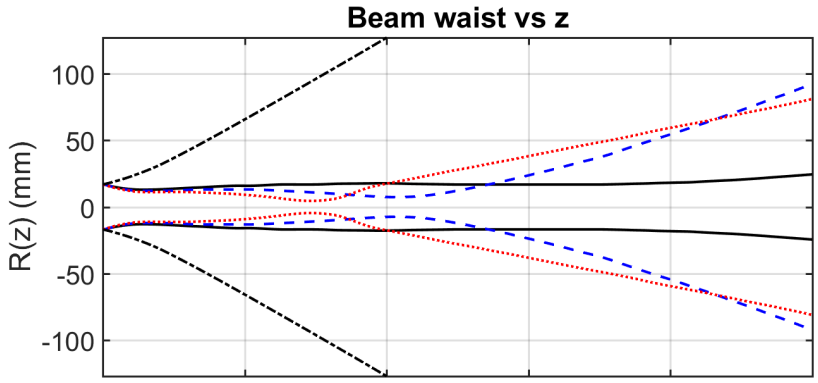

Figure 12 shows the evolution of the beam FWHM for the different cases depicted in Fig. ###. The 3 ps linear case (dash-dot) shows strong diffractive spreading and has a Rayleigh range of about 300m. The 2.4 ps results shows an initial focusing followed by diffractive spreading. Finally, the 3 ps case with many-body physics included shows a near constant waist beam over the full propagation range.

Breakdown of Avalanche Ionization Model – Two Temperature Plasma Model

Avalanche ionization becomes significant when USP durations exceed a few picoseconds. Traditionally, electron generation via avalanche ionization is assumed to follow the pulse intensity envelope and the plasma density expected to obey the following equation.

$$\frac{dN}{dt} = \frac{\sigma}{E_p} IN$$

Here E_p is the bandgap energy, σ the cross-section for inverse Bremstrahlung, I the pulse intensity and N the electron density. This model was originally derived for condensed media but has been regularly applied to gases as well. While it proves adequate at near-IR wavelengths, it fails to correctly capture the physics at longer wavelengths especially at the wavelength of interest here, namely 10μm. It is clear that this model implies that plasma generations switches off after the pulse has passed. Recent experiments with a few ps CO_2 pulsed laser by the group at UCLA, working in conjunction with Brookhaven National laboratory scientists, exposed a novel dynamical behavior. This led us to revisit this theory and conclude that the above model was not correct for a dilute gas in this wavelength region. In a recent paper, "Memory effects in the long-wave infrared avalanche ionization of gases: A review of recent progress" by Wright, Ewan; Koch, Stephan; Kolesik, Miroslav; Moloney, Jerome, Reports on Progress in Physics (submitted 2019), we proposed a new two temperature plasma model that correctly captures the observed experimental behavior.

The essence of the model is that "hot" electrons generated via our many-body approach at temperature T_e take time to relax to a plasma temperature T_{pl}. This is the time required for a highly nonequilibriuam plasma to relax to a Fermi distribution at the plasma temperature. Moreover, electrons can now continue to be generated after the pulse has left. The equations below captures these memory effects.

$$\frac{dT_{pl}}{dt} = -\frac{(T_{pl} - T_e)}{\tau},$$

$$\frac{dT_e}{dt} = -\frac{(T_e - T_{pl})}{\tau} + \frac{2e^2\tau_e I(t)}{3k_B c\epsilon_0 m_e(1+(\omega\tau_e)^2)} - \frac{3k_B(T_e - T_{pl})^2}{\tau E_p}\left(1 - \frac{N}{N_0}\right),$$

$$\frac{dN}{dt} = \frac{N}{\tau}\cdot\frac{3k_B(T_e - T_{pl})}{E_p}\left(1 - \frac{N}{N_0}\right) + \frac{dN}{dt}\Big|_{source}$$

$$\frac{dN}{dt}\Big|_{source} = C_{MBI}E^4(t)\sqrt{\frac{E^2(t)+s}{E^2(t)}}$$

$$\frac{dJ}{dt} = \frac{e^2}{m_e}N(t)E(t) - \nu_e J.$$

The first three equations capture the dynamics of the coupled two temperatures and carrier density, where the free electrons are seeded by our fit (eqn(4)) to the microscopic result in Fig. ## . The input to the UPPE propagator is via the current density in the final equation.

A joint paper on this work was recently published in Nature Photonics [“Megafilament in air formed by self-guided terawatt long-wavelength infrared laser” Sergei Tochitsky, Eric Welch, Mikhail Polyanskiy, Igor Pogorelsky, Paris Panagiotopoulos, Miroslav Kolesik, Ewan M. Wright, Stephan W. Koch, Jerome V. Moloney, Jeremy Pigeon and Chan Joshi, Nature Photonics, 13, 41, 2019] where our model successfully accounted for the observed experimental observations. The experiment involved focusing the about 2.5-3mm so as to achieve a on the order of 15-20 Rayleigh ranges over the available 35-40 meter propagation length in the laboratory. The pulsed system output two sequential pulses of 3 ps duration with a separation of about 25 ps. The lead pulse was slightly above critical power with a peak power of around 1 TW. The secondary delayed was about half the amplitude of the first.

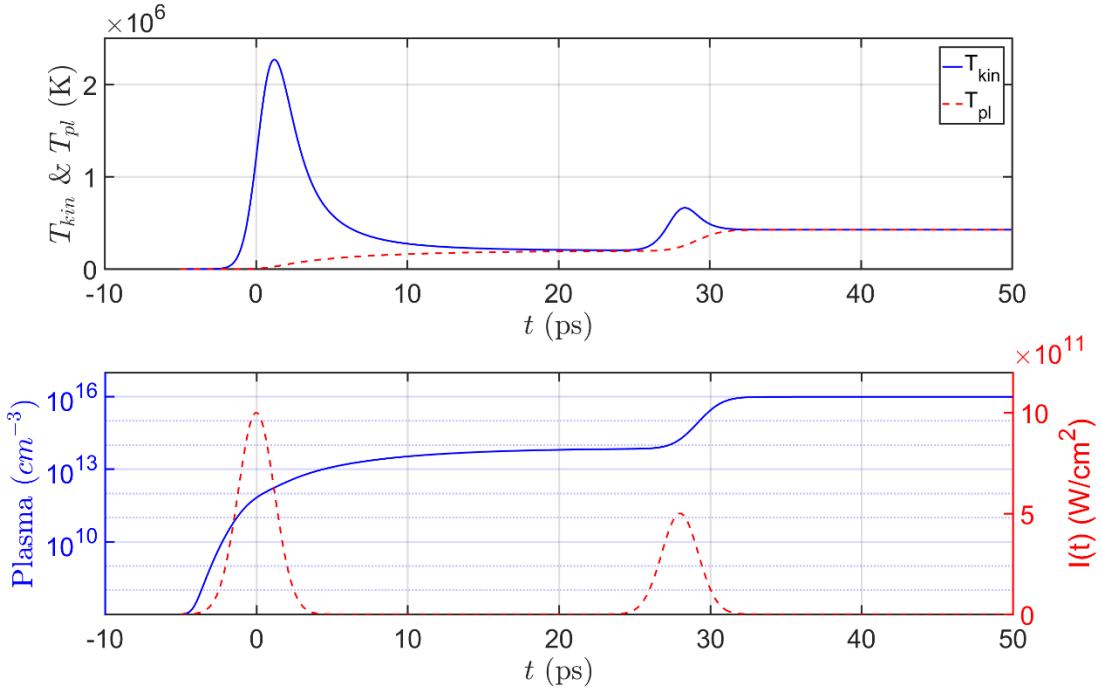

Figure 13 Top: Temporal representation of the hot electron temperature ($T_{e(kin)}$) and plasma temperature for a double pulse excitation. Bottom: Double pulses in dashed red and plasma density buildup over time.

Fig. 13 shows on the bottom the two pulse sequence (dashed red) and the corresponding plasma density in blue. The corresponding electron temperature (T_e) is shown in the top figure in blue and the plasma temperature to which it relaxes in red dashed. The key experimental observation was that the lead pulse (called a megafilament) stayed confined over 15 – 30 Rayleigh ranges. However, the second delayed pulse was seen to rapidly disappear after 5 meters from the focal spot. In this first 5 meters beyond the focal spot a bright plasma luminescence is observed. The physics responsible for this is clearly evident in the above Figure. In contrast to the conventional avalanche ionization model, the plasma buildup still continues after the first pulse and reaches a plateau before the second follow-on pulse arrives after 28 ps. The peak plasma density during the first pulse is low enough to suppress the Kerr lens via many-body effects without defocusing the pulse. At this stage, the second pulse though weaker, bumps the plasma density up to a level of around 10^{16} electrons per cm^3 at which point one should observe a bright plasma luminescence. The plasma density is now sufficient to defocus and terminate the second pulse.

Figure 14 shows the peak plasma density as a function of distance showing a maximum near the focal point at 0. The red arrow shows the 5 meter range over which plasma luminescence is observed in the experiment.

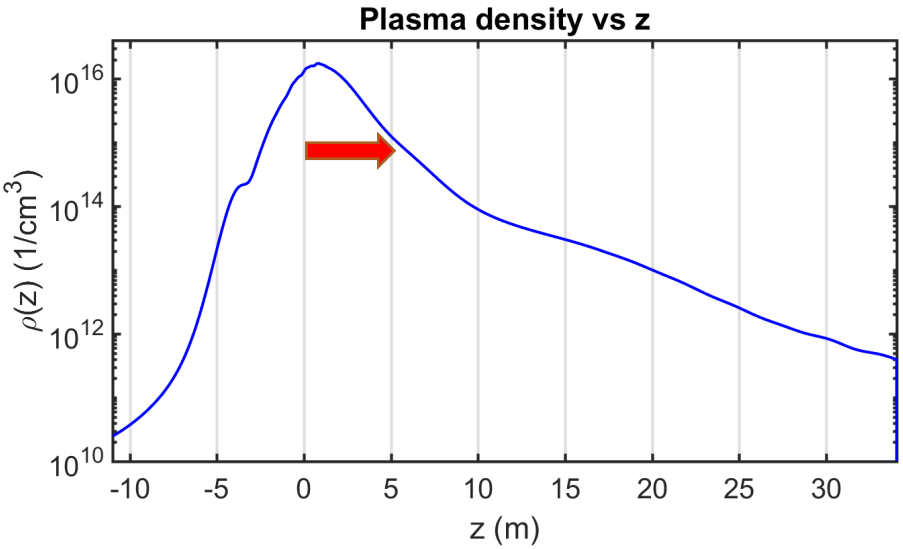

Figure 14. Full spatial dependence of the total plasma density over the full 30 m propagation range of the experiment.

Semiconformal FDTD Development - Applications to Metamaterials and Plasmonics

This project also supported the development of robust FDTD solvers capable of accurately resolving multiple arbitrary shaped nano-features in metamaterials, dielectrics and plasmonics. The figure below contrasts the gridding of a sphere with a nearby linear waveguide coupler which forms a key element in optical ring couplers. The linear waveguide can confine and transmit USPs while coupling them into micro-ring spherical resonators.

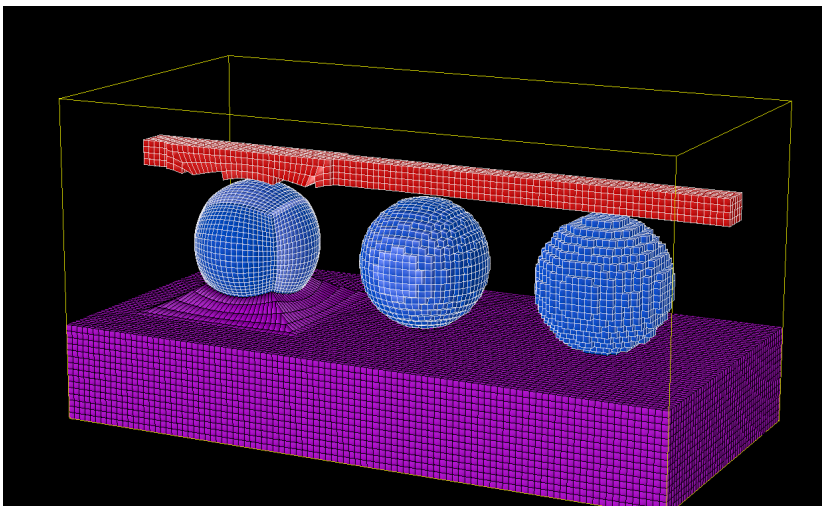

Figure 15 Schematic of different gridding for a 3D linear waveguide coupling to a sphere. Left: Conformal mesh, Middle: semi-conformal mesh and Right: Cartesian mesh

Figure 15 contrasts a conformal mesh where the mesh is conformal to the sphere but its region of influence pollutes the grid over that portion of the straight waveguide where accuracy in computing the near field is critical to calculating the coupling efficiency. On the right is a Cartesian mesh showing an irregular patterning on the sphere and consequently potential staircasing inaccuracies. The center part shows our semi-conformal mesh where a smooth gridding is maintained over the sphere and linear waveguide.

Another example shows 2D cut through a dimer of two metal nanospheres in Figure 16 with a very narrow spacing between them. Here, near-fields in the nanometer gap need to be accurately calculated for say, a molecular sensing application. The semi-conformal grid maps smoothly to both spheres, places a fine grid in the gap where a surface plasmon mode will, be generated and transitions into a regular Cartesian mesh away from the objects.

The general idea in mesh generation is to exploit transformation optics concepts and define a suitable grid transformation that keeps Maxell's equation invariant. This transformation of coordinates leaves Maxwell's equation invariant but at the cost of making the dielectric ε permittivity and magnetic permeability fully anisotropic tensors. Our first challenge therefore in implementing this new semi-conformal meshing scheme was to develop a stable second order convergent fully anisotropic FDTD solver.

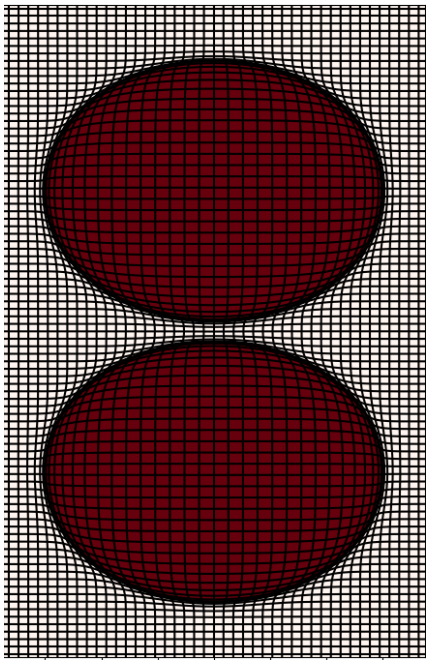

Figure 16. Semi-conformal mesh on metal dimers

We have developed a new fully-anisotropic 3D FDTD Maxwell solver for arbitrary electrically and magnetically anisotropic media for piecewise constant electric and magnetic materials that are co-located over the primary computational cells. Two numerical methods were developed that are called non-averaged and averaged methods, respectively. The non-averaged method is first-order accurate, while the averaged method is second-order accurate for smoothly-varying materials and reduces to first order for discontinuous material distributions. For the standard FDTD field locations with the co-location of the electric and magnetic materials at the primary computational cells, the averaged method required development of the different inversion algorithms of the constitutive relations for the electric and magnetic fields. We provide a mathematically rigorous stability proof followed by extensive numerical testing that includes long-time integration, eigenvalue analysis, tests with extreme, randomly placed material parameters, and various boundary conditions. For accuracy evaluation, we have constructed a test case with an explicit analytic solution. Using transformation optics, we have constructed complex, spatially inhomogeneous geometrical object with fully-anisotropic materials and a large dynamic range of $\underline{\epsilon}$ and $\underline{\mu}$, such that a plane wave incident on the object is perfectly reconstructed downstream. This work is published in the paper by Nehls J, Dineen C, Liu J, Poole C, Brio M, Moloney JV. Stable 3D FDTD method for arbitrary fully-electric and magnetic anisotropic Maxwell's equations. *Int J Numer Model*. 2018;e2521.https://doi.org/10.1002/jnm.2521

Applications to Metamaterials and Plasmonic Structures.

Designing the shape of silicon nanoparticles has been shown to be an effective approach to increasing overlap between electric and magnetic dipole resonances thereby achieving directional scattering and decrease of reflection. Variations of disk diameter and/or height affect resonances differently and can thus result in resonance overlap. In most of the studies, the disks are arranged in a periodic array where the periodicity is varied together with disk diameter, but the role of lattice effect is neglected. Here we theoretically study a periodic array of disks and show that the contribution of the lattice effect in shifting resonance positions is comparable to the effect of the diameter change. We demonstrate that the lattice effect is important even when the wavelength of diffraction remains on the blue side from electric and magnetic dipole resonances and there are no additional lattice resonances are excited. Period and disk dimensions are chosen so that the resonances overlap in the proximity of the telecommunication wavelength which is of great practical interest.The work is published in: V.E. Babicheva and J. Moloney, "Lattice effect influence on the electric and magnetic dipole resonance overlap in a disk array," Nanophotonics 7(10), 1663-1668 (2018).

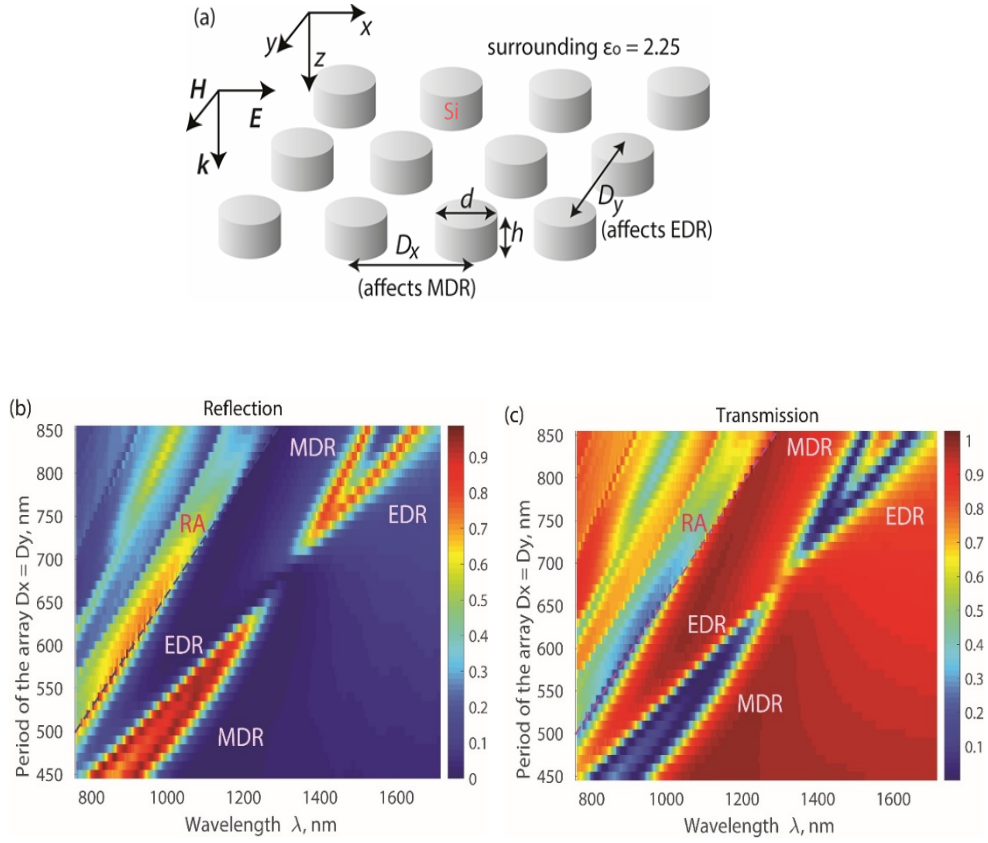

Figure 17 (a) Schematics of the structure under consideration: periodic array of disks and normal incidence of the light with the E field along the x-axis. Surrounding medium has $\varepsilon_o = 2.25$. For this polarization, the array period in the x-direction D_x affects excitation of a magnetic dipole resonance (MDR), and the period in y-direction D_y affects the electric dipole resonance (EDR). (b) Reflection and (c) transmission through the disk array under variation of the array periods and disk diameters with $D_x = D_y = d + 200$ nm. The dashed blue and red lines mark the Rayleigh anomaly wavelength $\lambda_{RA} = D_x = D_y$.

Optical resonances in isolated nanoparticles made out of commonly occurred materials with high optical losses, such as transition metal dichalcogenides, germanium, carbide, and others, are weak and do not sufficient field enhancement to compete with plasmonic resonances in noble metal nanoparticles. This work presents a novel approach to achieve strong resonances in the arrays of such nanoparticles with large optical losses and points to their potential for efficient light control in metasurfaces, ultra-flat optical elements, sensing, and photovoltaic applications. Materials with large imaginary part of permittivity (LIPP) are studied and nanostructures of these materials have shown to support not only surfaces modes, known as Zenneck waves, but also modes localized on the subwavelength particle. This approach opens up the possibility to excite strong nanoparticle localized resonances without involving plasmonic or high-refractive-index material. Arranging LIPP particles in the array plays a crucial role allowing for collective array resonances, which are shown to be much stronger in particle array than in single particle. The collective lattice resonances can be excited at the wavelength defined mainly by the array period and thus easily tuned in a broad spectral range not being limited by particle permittivity, size, or shape. This work is published in: V.E. Babicheva and J. Moloney, "Lattice Zenneck modes on subwavelength antennas," Laser & Photonics Reviews 12, 1800267 (2019).

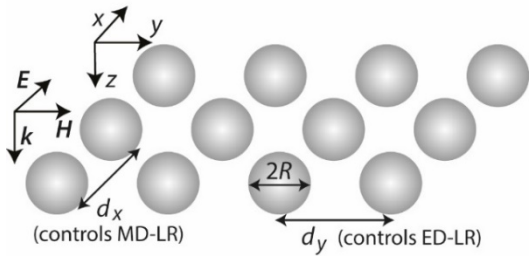

Figure 18 Periodic array of spherical particles with high imaginary part of permittivity (HIPP). Spherical particles have radius *R* = 100 nm. Light incidence is normal to the array plane and polarization *E* is along the x-direction. For this polarization, the array period in x-direction d_x controls excitation of magnetic dipole lattice resonance (MD-LR), and the period in y-direction d_y controls electric dipole lattice resonance (ED-LR).

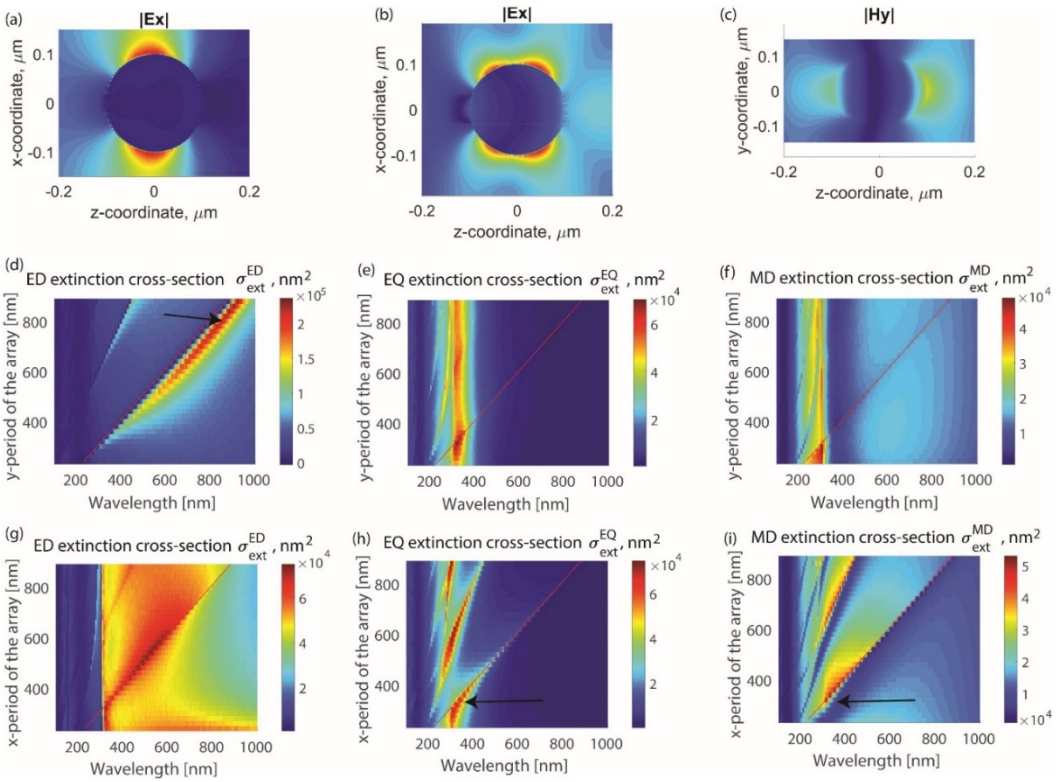

Figure 19 Excitation of ED, EQ, and MD multipole resonances in HIPP nanoparticle array. (a)-(c) Results of the FDTD numerical simulations of the modes: (a) ED-LR for d_x = 300 nm, d_y = 800 nm, λ = 840 nm, (b) and (c) are EQ-LR and MD-LR, respectively, for d_x = 390 nm, d_y = 300 nm, and λ = 395 nm. (d)-(i) Extinction cross-sections of ED, EQ, and MD multipoles calculated with coupled dipole-quadrupole equations for the variations of d_x (panels (d) to (f), fixed d_y = 300 nm) and d_y (panels (g) to (i), fixed d_x = 300 nm). Red solid lines denote Rayleigh anomaly wavelength. Black arrows on panels (d), (h), and (i) indicate what parameters are taken to simulate resonances in (a)-(c). Calculations are performed for an array of spheres with R = 100 nm and ε = 1 + 18i.

Transitions

During the development and application of our UPPE propagation code, we worked closely with Dr Victor Hasson who was supported on the project, to transition our new LWIR propagation results to DOD scientists. Dr. Hasson has been instrumental in promoting the development of a CO_2 USP source by an NRL/AFRL team that we anticipate can be employed at range to test our predictions. Through a contact with Dr Jennifer Elle, DR-02 USAF AFMC AFRL/RDHP we have also facilitated transitioning of the code to Dr. Ryan Phillips, RYAN E CTR USAF AFMC AFRL/RDHP.